Cerenkov Radiation Detection using 61 Pixel DEP Hybrid Photodiodes

by

Jesse D. Wodin

Submitted to the Department of Physics
in partial fulfillment of the requirements for the degree of

Bachelor of Science in Physics

at the

MASSACHUSETTS INSTITUTE OF TECHNOLOGY

June 2000

Author . . . .
Department of Physics
May 2000

Certified by . . . .
Peter Fisher
Associate Professor
Thesis Supervisor

Accepted by . . . .
David Pritchard
Chairman, Undergraduate Committee

Cerenkov Radiation Detection using 61 Pixel DEP Hybrid Photodiodes

by

Jesse D. Wodin

Submitted to the Department of Physics
on May 2000, in partial fulfillment of the
requirements for the degree of
Bachelor of Science in Physics

Abstract

The 61 pixel hybrid photodiode (HPD) as a photo - detector is studied. First, the light response of the HPD is investigated, revealing the single photon sensitivity of the HPD. Next, the behavior of the HPD in a magnetic field is studied. The predicted behavior of the HPD matches closely with what is observed. Lastly, the HPD is used to image Cerenkov rings from relativistic electrons passing through an aerogel radiator. The Cerenkov cone radii and index of refraction of the aerogel are reconstructed from this data. Two separate methods of fitting the Cerenkov cone agree and give an index of 1.148 ± 0.005 for the aerogel radiator, which agrees with the aerogel manufacturer's specifications.

Thesis Supervisor: Peter Fisher
Title: Associate Professor

Acknowledgments

The author would like to thank Peter Fisher, Fred Coté, Mike Grossman, Alan Rudge, Heinz Pernegger, Dave Custer, Craig Watkins, Jesse Kirchner, Bilge Demirköz, Elina Brobeck, Benjamin Monreal, Reyco Henning, Julie Wyatt, Yoshi Uchida and the MIT wire bonding lab.

Contents

List of Figures

List of Tables

Chapter 1

Introduction

Cerenkov radiation is produced when a charged particle moves through a transparent medium faster than the speed of light in that medium. The radiation is emitted in a cone (the Cerenkov cone) with central angle θ_C. Measurement of this angle leads to determination of the momentum of the particle, if the index of refraction of the medium is known. Conversely, if the momentum of the particle is known, the index of the refraction of the radiator can be reconstructed.

Cerenkov radiation was discovered in the 1930s, but came into wide use in particle physics during the 1950s. For a good historical account of the use of Cerenkov imaging in physics, see [7], (Chapter 1). Today, it is used in experiments such as BaBar at Stanford, and is proposed to be used on the Alpha Magnetic Spectrometer (AMS[1]) [1] for particle identification. The current proposition on AMS is to have a layer of material (called a radiator) which is especially made for producing Cerenkov radiation. Relativistic cosmic particles passing through this radiator will produce Cerenkov radiation. By imaging these rings using photo-detectors, the momentum of these particles can be determined.

The purpose of this thesis is to investigate the use of a new type of photo-detector in measuring Cerenkov rings. This photo-detector is called a hybrid photodiode (HPD). It is a hybrid vacuum tube - solid state silicon device for photo-detection.

[1] The purpose of AMS is to search for cosmic anti-particles. AMS is currently scheduled to be placed on the International Space Station in 2003

The face of the detector consists of 61 pixels, each with 2mm^2 active photon detection area. The photocathode on the detector is optimized for blue and UV light, which are the dominant frequencies of Cerenkov radiation.

The study of the photo - response of the HPD is presented in chapter 3. The behavior of the HPD in a magnetic field is presented in chapter 4 (see §4.1 for motivation behind this). Finally, the HPD was put into a beam line at the Bates Linear Accelerator Center. Cerenkov radiation was produced when relativistic electrons passed through an aerogel radiator. This radiation was detected by the HPD, and the index of refraction[2] of the radiator is reproduced to an accuracy of 0.005.

[2]It is known that n = 1.14 for the aerogel used in this experiment, as given by the manufacturer's specifications.

Chapter 2

Theory

2.1 Cerenkov Radiation and the Polarization Field

Consider a relativistic ($\beta \approx 1$) charged particle incident upon a material. We would like to look at how the particle interacts with the material. The dominant effect will be a Coulomb interaction between atomic electrons and the incoming particle. Assume the incident particle interacts with one atomic electron at impact parameter b. Then, we have a picture like this:

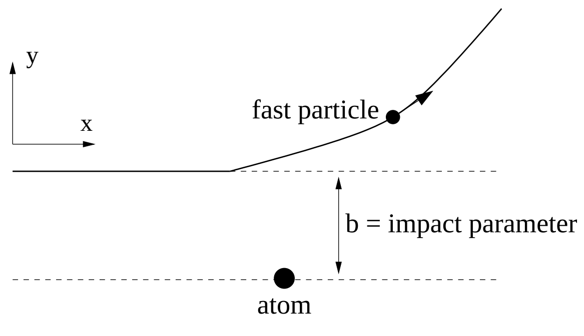

Figure 2-1: Coulomb scattering of fast particle off of an electron.

(Throughout this paper, the x and y directions are taken as shown in this figure.) Next, account for the possibility that the material is dense. This is done by assuming that there are many other atomic electrons between the incoming particle and the atomic electron in question. These other electrons will be influenced by the incoming particle's fields. The electrons will in turn cause perturbing fields at the original atom's position. This is the polarization field, caused in this case by the incoming particle. For close collisions (small impact parameter b: no atomic electrons between the incoming particle and atom in question), the polarization field can be ignored. For distant collisions (large impact parameter b: many atomic electrons between the particle and atom in question), the polarization field is not negligible, and will be treated macroscopically by considering the effect of the material's dielectric constant $\epsilon(\omega)$ on the fields.

The problem is to find the fields far from the incoming fast particle, which is moving with constant velocity v. These fields will comprise coherent radiation wavefronts at a large distance a ($a \gg b$). This is Cerenkov radiation. Further, the geometrical aspects of the field will be investigated, leading to the famous Cerenkov relation. This relates the spatial distribution of radiation (the Cerenkov cone) with the velocity v of the incoming particle and the index of refraction $n(\omega)$[1] of the material. Cerenkov radiation is emitted in a cone about the incoming particle's path, with central angle θ_C (see figure 2-2).

$$\cos\theta_c = \frac{1}{\beta n(\omega)} \tag{2.1}$$

θ_c is the polar emission angle, which is measured with respect to the axis of the incoming particle. $\beta = \frac{v}{c}$ corresponds to the incoming particle, and n is the index of refraction of the material through which the particle is passing.

2.2 Calculation of the fields

The central quantity in this calculation is the dielectric constant $\epsilon(\omega)$ of this material. Since ϵ is a function of frequency, it is convenient to work out fields in frequency space. The approach to finding the radiation field will be to:

1. Find the potentials $\phi(\vec{k},\omega)$ and $\vec{A}(\vec{k},\omega)$ from the wave equations in a dielectric.

[1] $n(\omega)$ is related to the dielectric constant of the material by $n(\omega) = \sqrt{\epsilon(\omega)}$

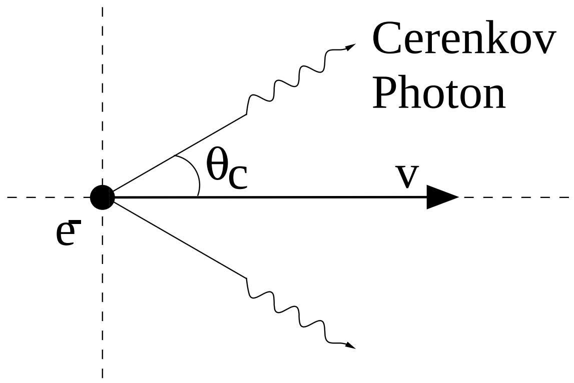

Figure 2-2: Cerenkov cone of a relativistic electron.

2. Represent the incoming particle as a delta function source to these wave equations.

3. Find the resulting fields, $\vec{E}$ and $\vec{B}$.

4. Find the energy loss by the incoming particle to an electron on an atom in the material. This will be the energy radiated away (Cerenkov radiation) by the particle as it passes through the medium.

5. Use the fields to deduce the radiation pattern (which will turn out to be a cone with central angle θ_C).

The wave equations for the potentials in a medium with dielectric constant $\epsilon(\omega)$, are

$$\left(\nabla^2 + \frac{\epsilon(\omega)}{c^2}\frac{\partial^2}{\partial t^2}\right)\phi(\vec{x},t) = \frac{4\pi}{\epsilon(\omega)}\rho(\vec{x},t) \tag{2.2}$$

$$\left(\nabla^2 + \frac{\epsilon(\omega)}{c^2}\frac{\partial^2}{\partial t^2}\right)\vec{A}(\vec{x},t) = \frac{4\pi}{\epsilon(\omega)}\vec{J}(\vec{x},t). \tag{2.3}$$

The source equations of an incoming particle with constant velocity v and charge ze are

$$\rho(\vec{x},t) = ze\delta(\vec{x} - \vec{v}t) \tag{2.4}$$

$$\vec{J}(\vec{x},t) = \vec{v}\rho(\vec{x},t). \tag{2.5}$$

The Fourier transforms of the potentials can be solved in terms of the sources:

$$\phi(\vec{k},\omega) = \frac{2ze}{\epsilon(\omega)} \frac{\delta(\omega - \vec{k}\cdot\vec{v})}{\left(k^2 - \frac{\omega^2}{c^2}\epsilon(\omega)\right)} \tag{2.6}$$

$$\vec{A}(\vec{k},\omega) = \epsilon(\omega)\frac{\vec{v}}{c}\phi(\vec{k},\omega). \tag{2.7}$$

From these expressions the fields can be calculated, using $\vec{B} = \vec{\nabla}\times\vec{A}$ and $\vec{E} = -\vec{\nabla}\phi$.

$$\vec{E}(\vec{k},\omega) = i\left(\frac{\omega\epsilon(\omega)}{c}\frac{\vec{v}}{c} - \vec{k}\right)\phi(\vec{k},\omega) \tag{2.8}$$

$$\vec{B}(\vec{k},\omega) = i\epsilon(\omega)\vec{k}\times\frac{\vec{v}}{c}\phi(\vec{k},\omega) \tag{2.9}$$

2.3 Energy Loss ($\frac{d\mathcal{E}}{dx}$): The Spectral Distribution of Cerenkov Radiation

The time derivative of the work done on the atomic electron by the incoming particle is the energy loss of that electron (see [5], p. 634). A more geometrical (and clever) way to calculate the energy loss is to realize that the Coulomb interaction between these particles will cause the fast particle to lose energy. Then, by conservation of energy, it suffices to calculate the flow of energy through a cylindrical surface (radius a) about the path of the particle. This is the integral of the Poynting vector, $\vec{S} = \frac{c}{4\pi}\vec{E}\times\vec{B}$, over the cylinder, and will yield $\frac{d\mathcal{E}}{dt}$ (the energy loss per unit time). By symmetry,

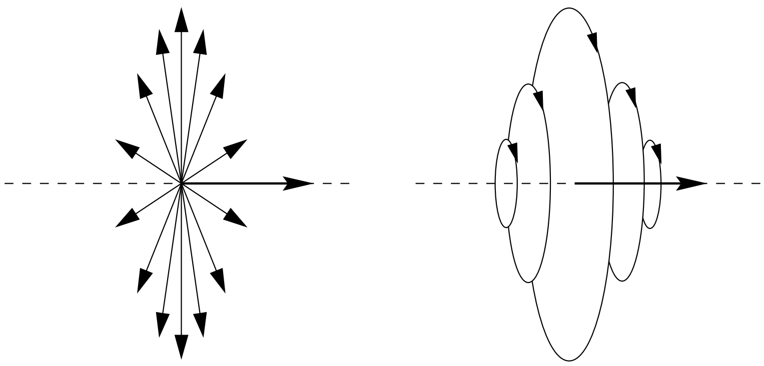

Figure 2-3: Electric and magnetic fields of a charge moving with constant velocity v.

only the y - component of the Poynting vector has to be integrated. The energy loss per unit distance is therefore

$$\frac{d\mathcal{E}}{dx} = \frac{1}{v}\frac{d\mathcal{E}}{dt} = -\frac{c}{4\pi v}\int_{-\infty}^{\infty} 2\pi a B_z E_x dx. \tag{2.10}$$

This integration is done in detail in [5] (pp. 632 - 634). We define a new parameter λ in the integration

$$\lambda = \sqrt{\frac{\omega^2}{v^2}\left(1 - \beta^2\epsilon(\omega)\right)}. \tag{2.11}$$

λ characterizes the density effect and has units of *length*$^{-1}$ (see [5], pp. 624 - 640 for a detailed description). As β gets large, the particle interacts with the material more. This causes λ to have an increasingly large complex component, which will mathematically allow for energy to escape to infinity as radiation.

Assuming that $\epsilon(\omega)$ is purely real (no absorbtion), the invariance of the result of equation 2.10 under the transformation

$$\lambda = -i|\lambda| \tag{2.12}$$

(see [5], pp. 632 - 634) leads to the result,

$$\beta^2\epsilon(\omega) > 1. \tag{2.13}$$

Rewritten,

$$v > \frac{c}{n}, \tag{2.14}$$

is the condition required for Cerenkov radiation to occur. *The velocity of the fast particle must be greater than the speed of light in the material in order for Cerenkov radiation to be emitted.*

The energy loss becomes

$$\frac{d\mathcal{E}}{dx} = -ca\int_0^{\frac{c\pi}{r_e}} \frac{z^2e^2}{c^2}\omega\left(1 - \frac{1}{\beta^2\epsilon(\omega)}\right)d\omega\bigg|_{\beta^2\epsilon(\omega)>1}, \tag{2.15}$$

where r_e is the classical radius of the electron. The upper limit on the integral is one over the time it takes for information to travel from one side of the electron to the other. The electron cannot radiate at any frequency higher than this (see [6]).

This is the result first published by Frank and Tamm in 1937, giving the frequency spectrum of Cerenkov radiation emitted from a material with dielectric constant $\epsilon(\omega)$, due to an incoming particle with velocity $v = \beta c$.The form of $\epsilon(\omega)$ along with condition 2.13 make the integral finite. The general form of $\epsilon(\omega)$ is

$$\epsilon(\omega) = 1 + \frac{4\pi N e^2}{m_e} \sum_j \frac{f_j}{\omega_j^2 - \omega^2 - i\Gamma\omega} \tag{2.16}$$

where the f_j's are material resonances, ω_j's are atomic resonances, and Γ is a damping term accounting for absorption (see [3], §30-32). Together with equation 2.13, this gives a radiation yield for frequencies in the region shaded below.

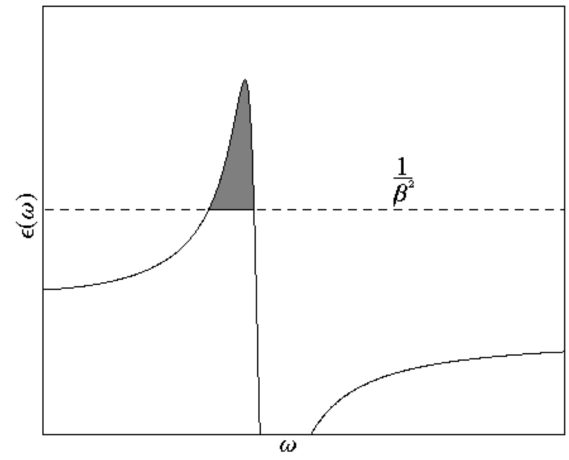

Figure 2-4: Cerenkov radiation region: $\beta^2\epsilon(\omega) > 1$.

2.4 Spatial Distribution of Cerenkov Radiation: The Cerenkov Cone

The electric and magnetic fields (equations 2.8 and 2.9) for distances large compared to the impact parameter, have components like those shown in figure 2-5. The

Cerenkov angle θ_c is given by

$$\cos\theta_c = \frac{E_y}{\sqrt{E_x^2 + E_y^2}}, \tag{2.17}$$

which when simplified becomes

$$\cos\theta_c = \frac{1}{\beta n(\omega)}, \tag{2.18}$$

which reestablishes equation 2.1. From this picture, Cerenkov radiation is released in a cone with a polar emission angle θ_c. It is also linearly polarized in the plane containing the direction of observation and the path of the particle ([5], p. 639). For

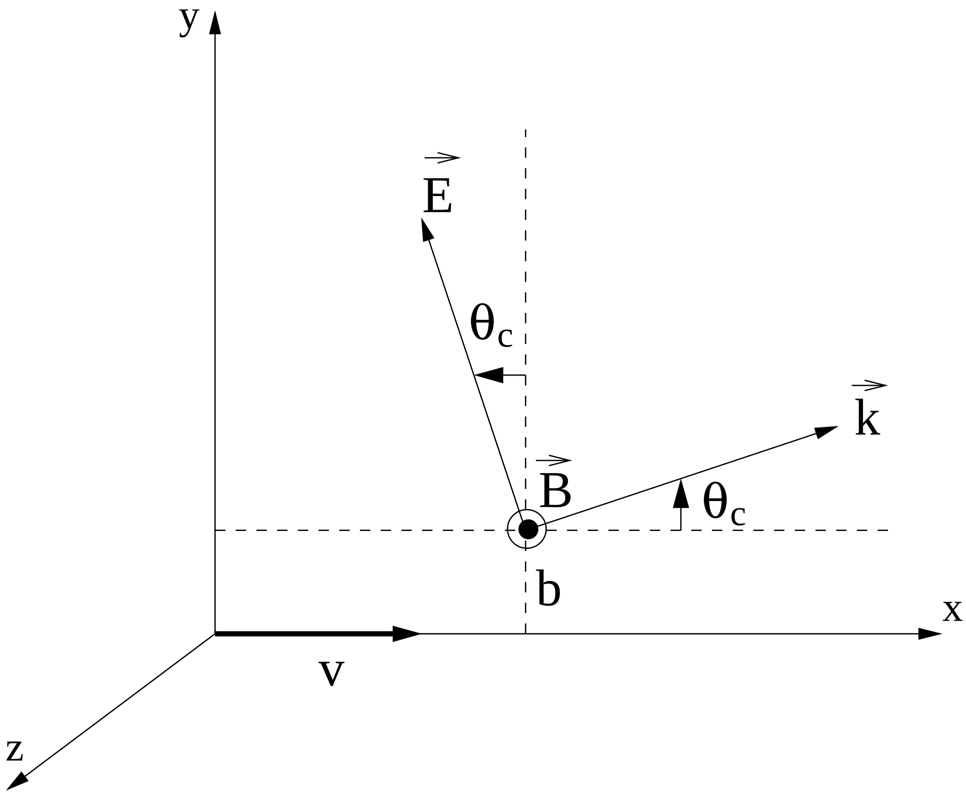

Figure 2-5: Geometry of Cerenkov radiation.

a material with known $\epsilon(\omega)$, the velocity of an incoming particle can be calculated by measuring the angle of the Cerenkov radiation cone. This makes Cerenkov radiation a useful tool for particle physics. In reality, $\epsilon(\omega)$ has many peaks like the one shown in figure 2-4. There will be some small spread in angles and frequencies of light emitted, but this will be limited by the frequency acceptance curve of the photo-detector. The photo-detector used here has a high quantum efficiency only for the green to UV range (200nm to 500nm wavelengths).

Chapter 3

Apparatus

3.1 The DEP Hybrid Photo Diode (HPD)

The DEP[1]HPD is a composite photo-detector/SI-PIN diode detector (see figure 3-1). Incident photons upon the HPD produce photoelectrons at the photocathode. These are accelerated and deposited in the depletion region of a back biased SI-PIN diode array (pixels). The signal from the photoelectrons may be read out from feedthrough pins on the back-side of the detector.

3.1.1 Physical Description

The HPD can be thought of as having two sections. The first section is an optical window, which is quartz-glass with a photocathode deposited on it. According to the manufacturer's specifications, the HPD used throughout this experiment had a 20% quantum efficiency between 200nm and 450nm. The quantum efficiency drops to 10% by 600nm and 1% by 800nm. Since Cerenkov radiation is mostly in the blue, the HPD is well suited to this application.

The second piece is a SI-PIN diode array, separated from the photocathode by approximately 13mm of vacuum. This array has 61 hexagonal pixels (see figure 3-1, front view, for pixel layout), each with an active area of 3.5mm^2. There is $100\text{M}\Omega$

[1]DEP is Delft Electronics Products, a company specializing in photo-detectors.

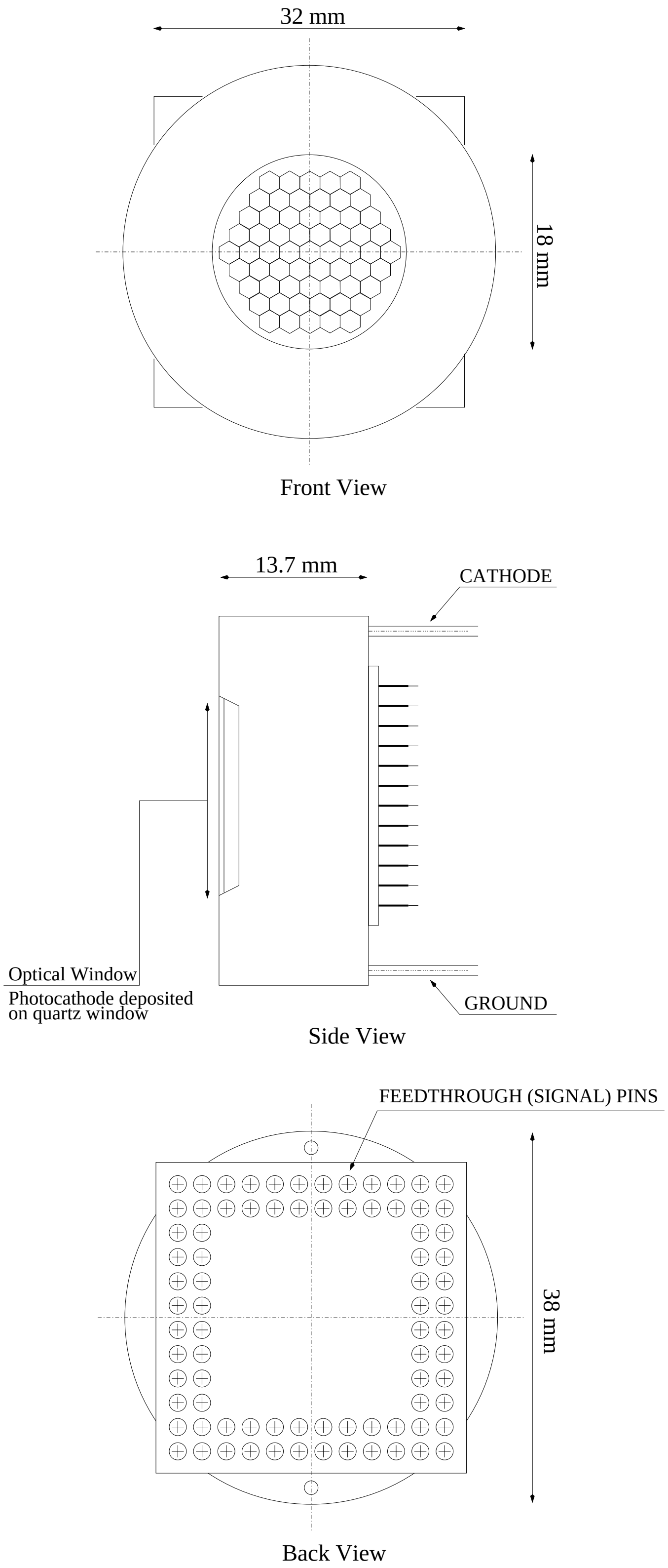

Figure 3-1: HPD Schematic.

resistance between each pixel, so each pixel is essentially isolated from the others. Furthermore, each pixel is reverse biased at +100V in order to allow holes created in the depletion region of the diode to be attracted towards the feedthrough pins. This allows for a signal to be read out by the preamp stage.

The HPD can be operated with anywhere from 0 to -12kV across the vacuum gap, but appreciable photon detection efficiency is only seen between -8kV and -12kV.

3.1.2 Signal Generation

A single photon (between 200nm and 450nm) incident upon the photocathode will produce a photoelectron (e^-) 20% of the time. If -12kV is applied across the HPD, then a single e^- nearly at rest at the photocathode will accelerate to 12keV by the time it hits a silicon pixel at the back end of the HPD. This electron will generate electron - hole pairs in the depletion region of the silicon. This will cause a reverse current to flow through the diode (due to the applied +100V bias) into a feedthrough pin on the back of the HPD. The current is directly proportional to the energy of the electron incident upon the diode. The average energy gap between the conduction band and the valence band of silicon is about 1eV, so a 12keV electron will produce approximately 12,000 e^- in the diode.

3.2 Readout and Data Acquisition System

The charge on the HPD diodes must be integrated, conditioned, and converted to digital levels for a computer to write to file. Charge integration, pulse shaping, and sample/hold is accomplished by the 128 channel VA chip (see figure 3-2 for complete DAQ chain). The integration time and pulse shaping parameters for the VA chip are controlled by adjustable voltages on the repeater card, shown in figure 3-2. Further amplification and noise filtering is done by the repeater card. Channels are digitized with a LeCroy 12-bit flash ADC (CAMAC), and sent to a computer through a standard GPIB interface. The computer is outfitted with LabView 5.0 and GPIB hardware for CAMAC interfacing.

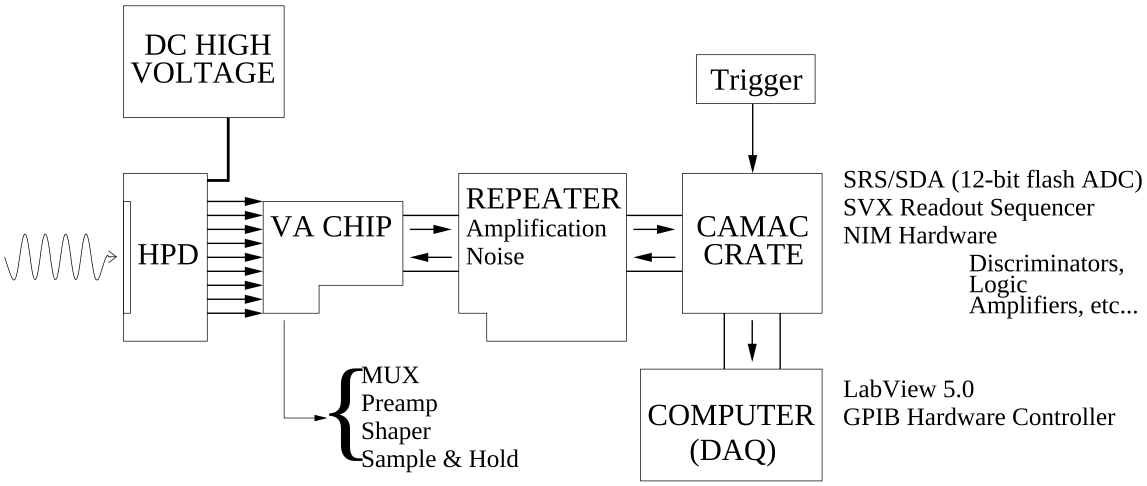

Figure 3-2: Readout and DAQ skeleton diagram.

3.2.1 VA Chip

The purpose of the VA (see figure 3-3 for a portion of the VA) is to convert a series of charge signals (Qin) into output analog voltage levels (Vout), which are fed into an amplifier and ADC. The VA chip is a monolithic IC specifically designed for solid state particle detector readout[2]. 61 of its 128 channels were connected between the HPD (61 pixels) and the VA.

The VA has two readout modes: single channel and multi-channel. Single channel mode is used to monitor one input channel out of a possible 128 on the VA. Single channel operation is used for calibration purposes (see chapter 3). Multi-channel operation allows for multiplexing of all 128 channels on the VA (normal operation), and is the mode used in reading out the HPD. For normal operation, the VA requires power, as well as timing signals for channel readout. The timing signals are programmed into the flash RAM of the SVX Readout Sequencer (CAMAC - see figure 3-2).

Upon receiving a trigger (e.g. from a possible physics event), the SVX sequencer passes all timing signals through the repeater card, and on to the VA. The VA then reads out the charge on each of the 61 HPD pins. Each signal is passed through a separate circuit like the one in figure 3-3. There are 128 of these circuits on the VA

[2]Supplied by IDEAS (Norway), using 1.2μm CMOS technology of AMS (Australia).

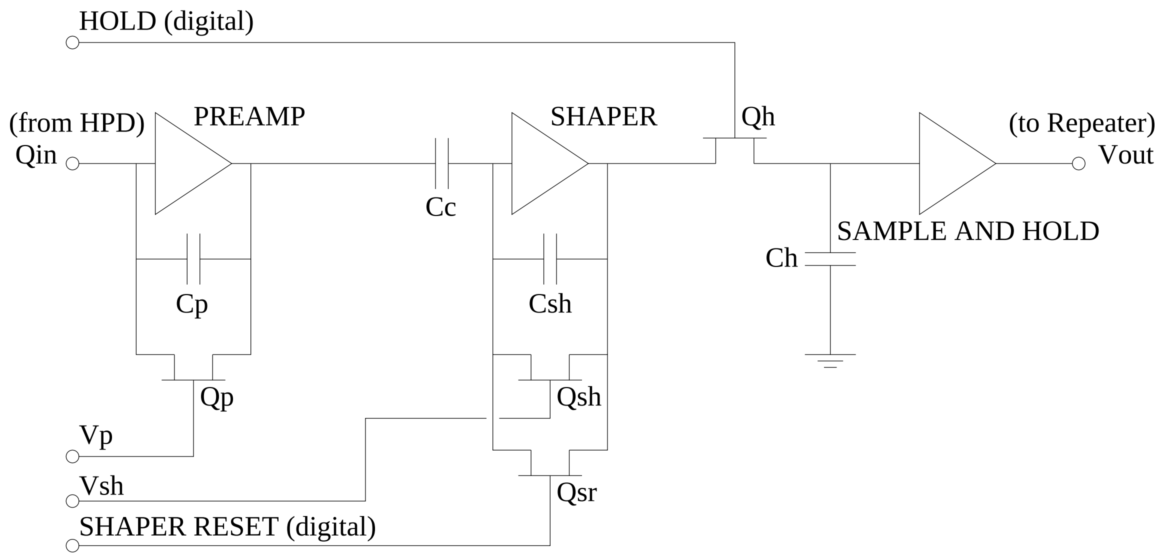

Figure 3-3: VA on board signal conditioning stages.

chip.

The VA signal conditioning stages are split into three parts: preamp, shaper, and sample/hold. First, charge from an HPD pixel is pulled across a bias (+100V) into Qin on the preamp. The charge is integrated across Cp. The Qp FET is adjustable (very large resistance), and is used to bleed off any bias current coming from the +100V bias supply. It also has the effect of preventing saturation during integration. The shaper stage is just a differentiator. The Qsh FET acts as a variable resistor, which changes the differentiation time constant of the circuit. The Csh capacitor is a standard solution to the unstable nature of differentiators (differentiators often are unstable at high frequencies, so this capacitor turns the circuit into an integrator in that region (see [4], p. 224)). The Qsr FET is a standard reset switch, used to drain any excess charge off capacitors Csh and Cc once this stage is finished. The final stage is the sample and hold stage. The shaper will push out a voltage to charge the Ch capacitor. The sample and hold op-amp then outputs a voltage proportional to the voltage across this capacitor, until the HOLD signal is sent to Qh. At this point, Ch is drained through the FET and the process begins again.

The purpose of the VA is to convert an input charge (Qin) into an output analog voltage level (Vout) to be fed into an amplifier and ADC. The VA integration time of the charge signal from the HPD was 2 μs.

Chapter 4

Calibration

4.1 VA and ADC Calibration

The VA chip and repeater card were calibrated by injecting a set amount of charge into each channel on the chip. This was done by charging up a 0.8pF capacitor with a square wave, and then discharging it into each channel. The voltage pulse was adjustable, giving known amounts of charge injected into each channel. The response of the chip was read out on an oscilloscope, producing the data (circles) in figure (4-1). This same signal was then measured at the output of the repeater card, to measure

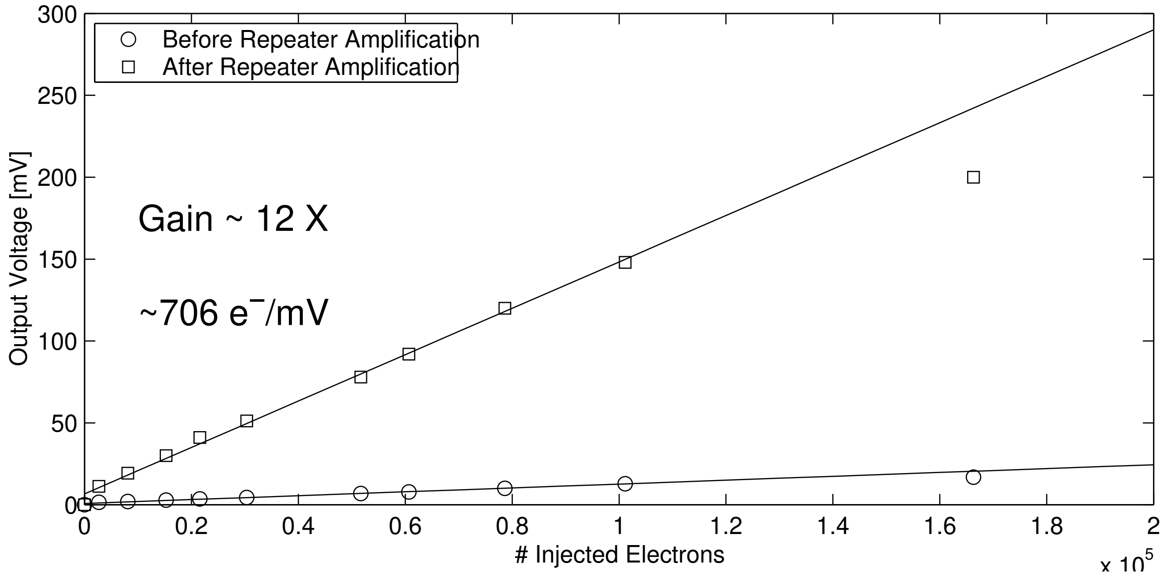

Figure 4-1: VA/Repeater calibration.

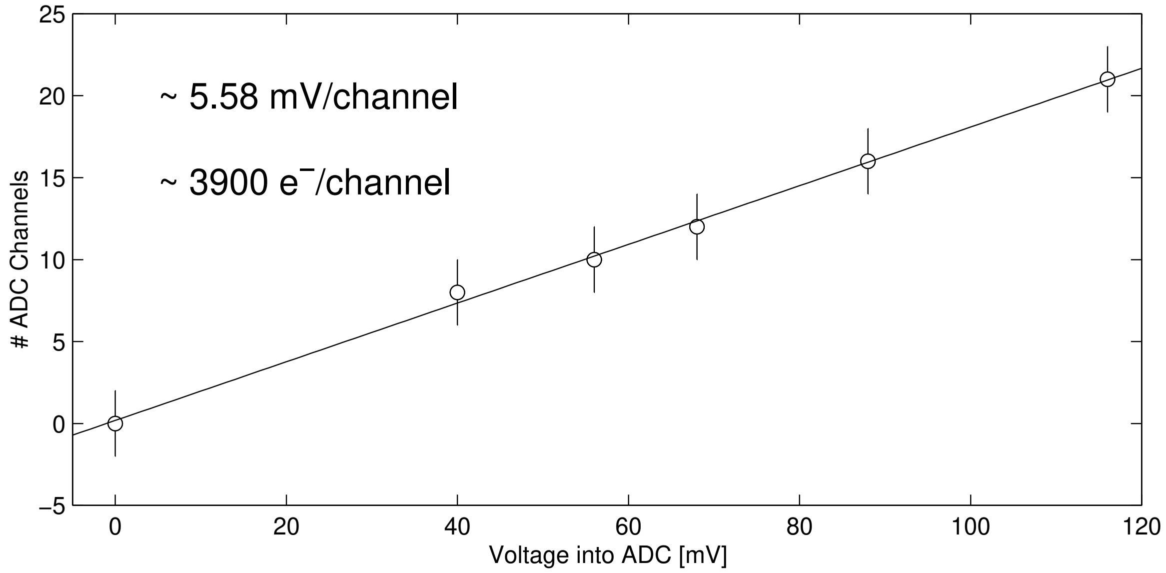

Figure 4-2: ADC calibration.

its amplification (squares). Data was taken for very small amounts of injected charge, in order to make sure that the chip was in the linear region (plateaus at high charge injection). These data points were fit by least squares to straight lines, giving a chip response and repeater gain ($\sim 12\times$). From this result, 706 injected e^- on the detector end of the VA gives a 1mV response at the output stage.

Next, set voltages were injected into the ADC, and the response of the ADC was measured, giving the data in figure (4-2). The data was fit by least squares, giving an ADC response of $5.58\frac{mV}{channel}$. From these two sets of data, *1 ADC channel corresponds to 3900e^- injected into the detector end of the VA. This means that 1 photon = 3 ADC channels.*

4.2 HPD Calibration

4.2.1 Light Detection and Integration Window

This test was made to see if the HPD detected light from an LED. A fiber optic line was held in place over one of the HPD pixels. The other end of the line was glued onto a green LED ($\sim$ 500nm). The LED was attached to an adjustable width pulse generator. The readout system was set up, the entire system was put in a light-proof

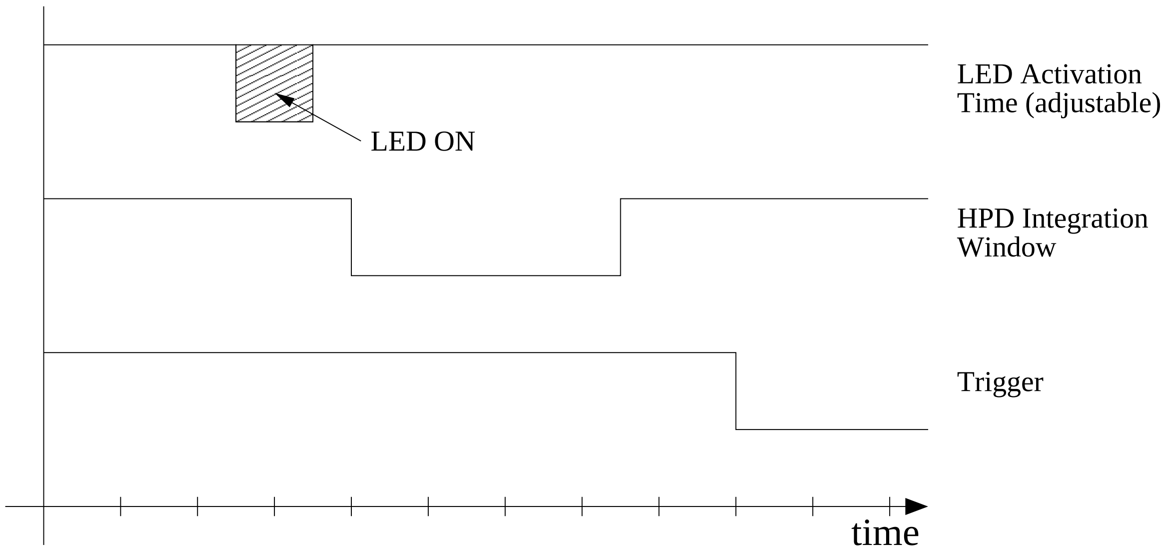

Figure 4-3: Timing diagram for HPD light integration window.

box, and the high voltage across the HPD was set to 12kV. The width of the input pulse to the LED was set to 120ns (a great deal of light). This light pulse was then sent to the HPD at different times (see figures 4-3 and 4-4). The time axis in figure 4-4 and the top time line in figure 4-3 correspond to the point at which the LED pulse was sent to the HPD with respect to the readout request time of the computer (bottom time line in figure 4-3). This data both established that the HPD responded to the light, and also the position of the window where the VA integrated charge from the HPD with respect to a trigger.

4.2.2 Linearity of HPD Response

After light response was established, the gain linearity of the HPD as a function of applied high voltage was measured. The response curve starts off at zero and curves up (see figure 4-5). Above 2kV, the response is linear, with a $\chi^2/$ d.o.f. of 0.84 (error bars too small to be visible on plot). The maximum suggested operating voltage of the HPD was 12kV.

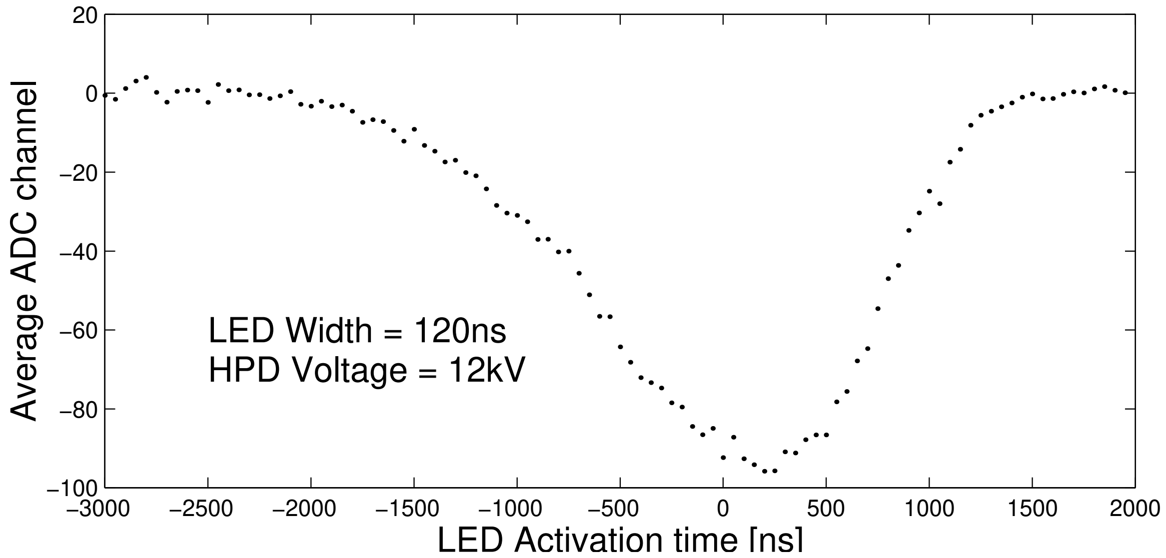

Figure 4-4: Integration window.

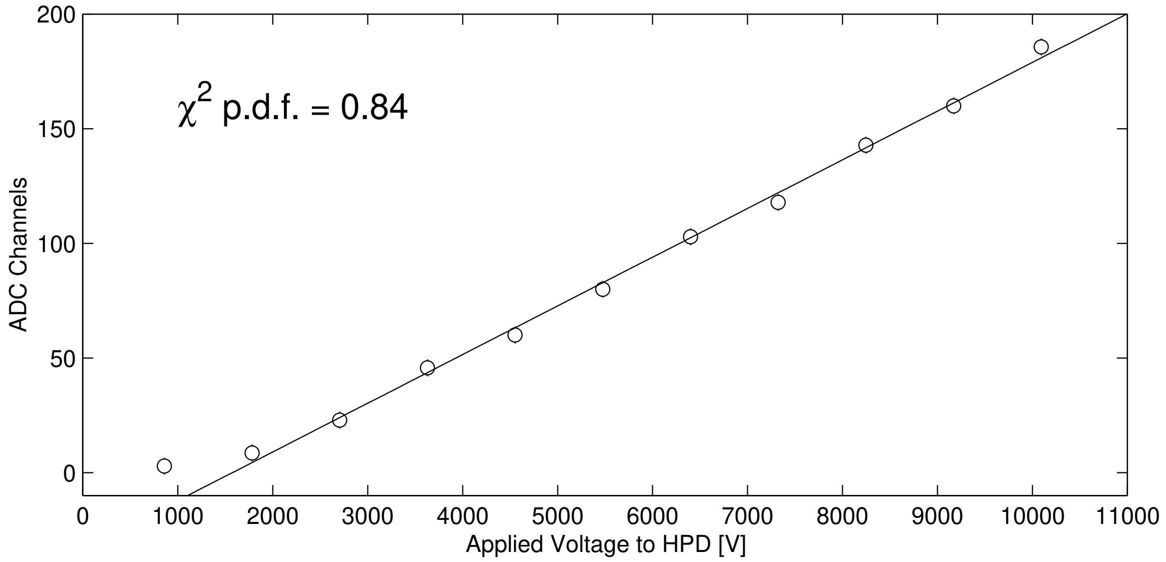

Figure 4-5: HPD light response as a function of high voltage.

4.2.3 Single Photon Response

The low light response of the HPD was tested. The setup was kept the same as above, with -12kV applied to the HPD. Low levels of light were injected by the LED/fiber setup into a single pixel on the HPD. The LED input pulse width was scanned from 30ns to 145ns in 5ns increments. At each width, 20,000 events (one event consists of two numbers: LED ON, LED OFF) were taken, producing the histograms in figure 4-6. The dotted histograms are the LED OFF data. The solid histograms are the LED ON data. At 30 ns, there is no noticeable difference between LED ON and LED OFF (30ns was not enough time for the LED to turn on). By 50ns, there is already a noticeable amount of light. This difference is quantized by subtracting the LED OFF data from the LED ON data and fitting the results to Poisson distributions to obtain the average number of photons detected as a function of LED width.

Production of photoelectrons at the photocathode of the HPD due to incident photons is a Poisson process. The probability that m photoelectrons will be produced given N_γ incident photons is given by

$$P(m\,e^-) = \frac{e^{-\lambda}\lambda^m}{m!}, \tag{4.1}$$

where $\lambda = N_\gamma p$ is the Poisson parameter, which gives the mean number of photons produced per incident photon. $p = 20\%$ is the quantum efficiency of the photocathode.

Assuming an incident photon produces a single e^- at the photocathode, it will become a 12keV e^- when it hits the silicon backplane (pixels). This will produce 12,000 e^-'s in the silicon. According to the calibration, *a width of 3 ADC channels corresponds to one incident photon.* For different LED widths (different amounts of light), distributions in figure 4-6 are produced. Each distribution is re-binned using the above calibration, giving distributions of number of photons versus number of counts. These were fit to Poisson distributions, giving the mean number of photons, N_γ, as a function of LED width. The fit values of N_γ are plotted in figure 4-7. The average $\chi^2/$ d.o.f. was 38. The low number of photons for these widths is due to several things: the weak optical coupling of the fiber to the LED; the weak coupling

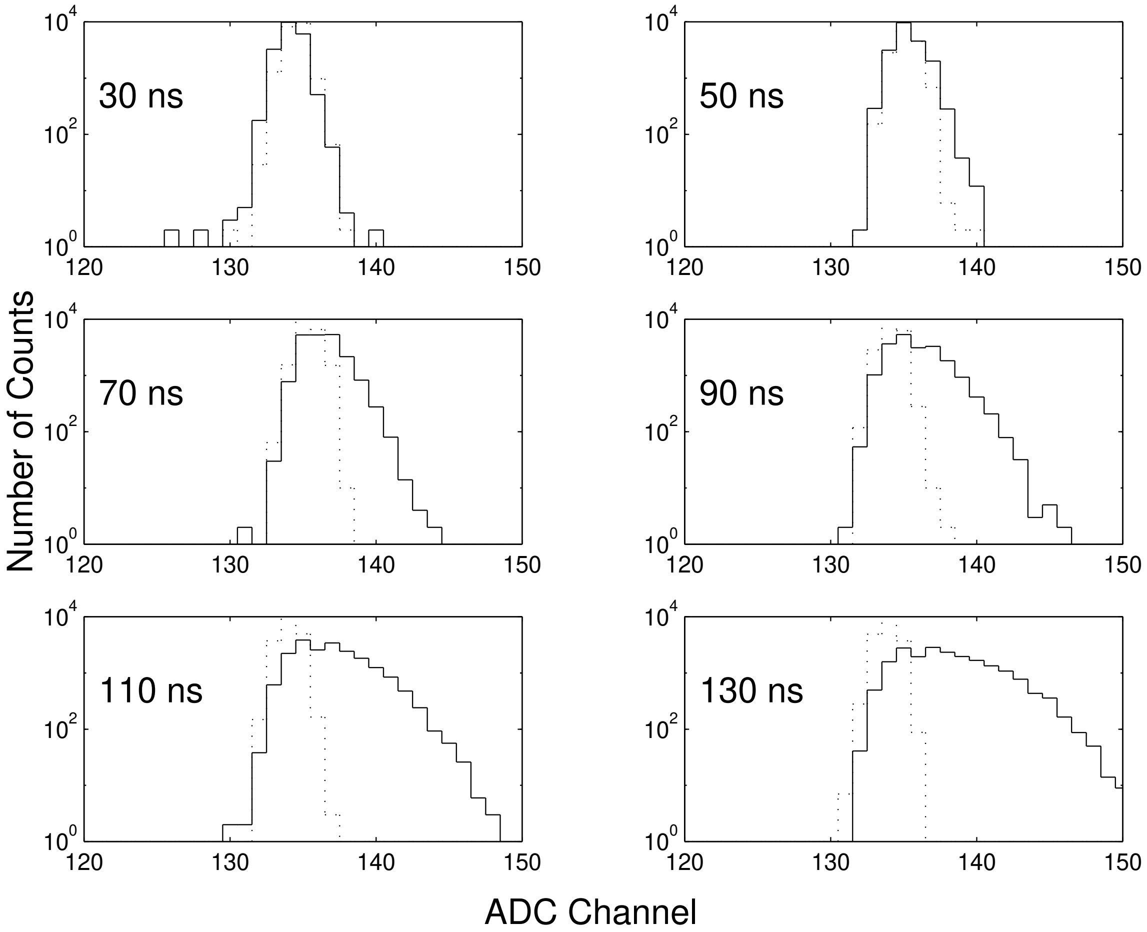

Figure 4-6: HPD light response (dotted = LED OFF; solid = LED ON).

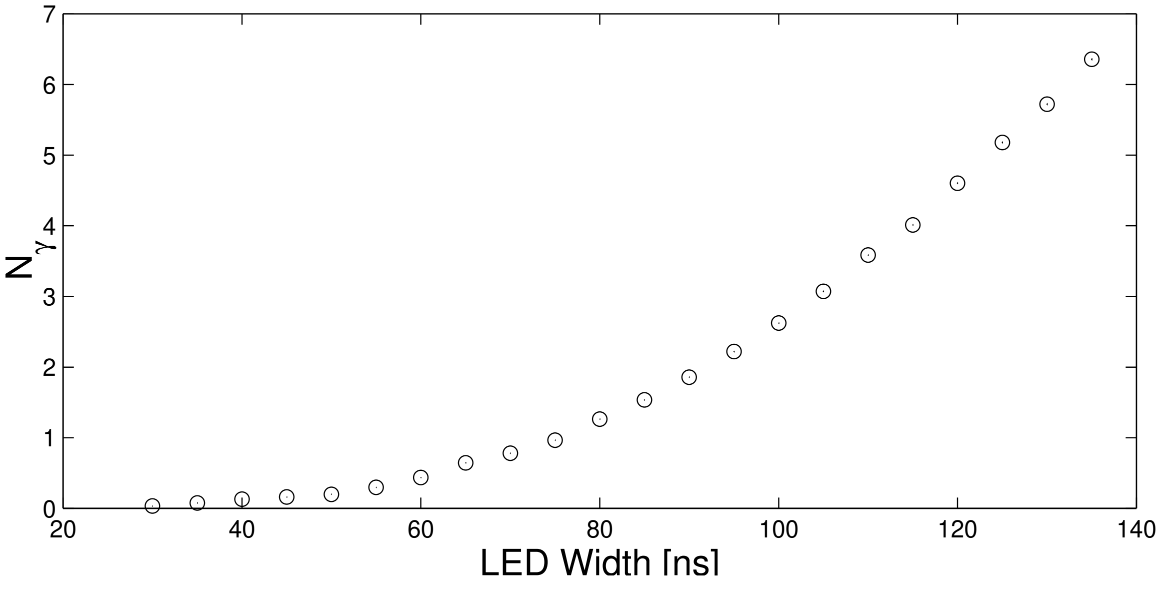

Figure 4-7: Average number of photons vs. LED width.

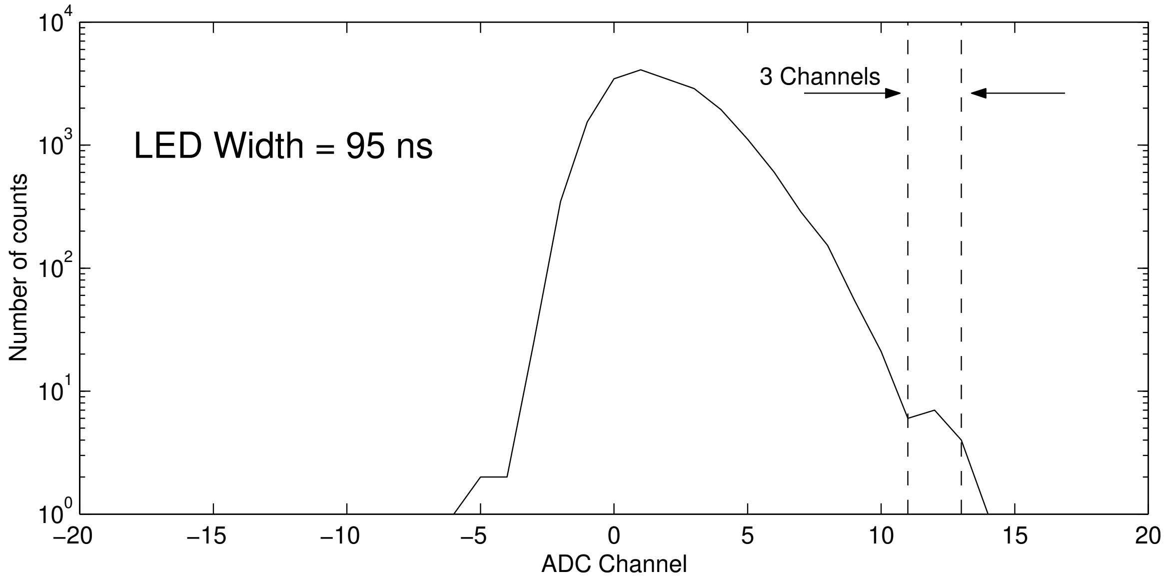

Figure 4-8: 5 Photon Shoulder.

of the fiber to the HPD quartz window; and the small optical surface area of the fiber. The goal was to get the least amount of light possible to the photocathode, in an attempt to see one photon at a time, so the fiber was deliberately badly coupled. The single photon peak was not clearly seen, as the amplification was not high enough. Nevertheless, shoulders in the histograms due to individual photons can be seen. In figure 4-8, the average number of photons from the Poisson fit is about 2, but the 5 photon shoulder can be seen.

Chapter 5

Behavior of the HPD in a Magnetic Field

5.1 Motivation

Many particle detection experiments require large magnetic fields for particle identification. Particles of opposite charge are identified by the difference in their tracks in the presence of magnetic fields. Conventional avalanche photo-tubes are unpredictable in magnetic fields, due to their complicated internal anode structure. They are not usually used in magnetic fields. The HPD vacuum gap amplification stage (the acceleration of the photoelectron across the -12kV) is composed of vacuum, so the path of the electron is predictable. If the HPD is set parallel to magnetic field lines, the electron will feel no magnetic force and accelerate in the direction of the internal field set up by the high voltage supply. If the magnetic field is in some other direction, the path of the photoelectron is still predictable, using the Lorentz force law.

5.2 Theoretical Prediction

The HPD works by accelerating photoelectrons (e^-) across the potential set up by a high voltage power supply. When an external magnetic field is applied, the path of the e^- inside the HPD will curve according to the Lorentz force law (see figure 5-1). A particle of charge e in $\vec{E}$ and $\vec{B}$ fields will experience a force

$$\vec{F} = e\left(\vec{E} + \vec{v} \times \vec{B}\right). \tag{5.1}$$

This second order differential equation can be solved parametrically, in the case of $\vec{E} \perp \vec{B}$. The solutions are

$$x(t) = \frac{E}{\omega B}\left[1 - \cos\left(\omega t\right)\right] \tag{5.2}$$

$$y(t) = \frac{E}{\omega B}\left[\omega t - \sin\left(\omega t\right)\right], \tag{5.3}$$

which are the equations of a cycloid, where $\omega = \frac{eB}{m_e}$ is the cyclotron frequency of the electron. Trajectories of the e^- following these equations are plotted in figure 5-1. This figure is looking sideways into the HPD, so light is incident at the top horizontal line. The solid curves are then the calculated trajectories of the photoelectrons at 10, 100, 200, and 300 Gauss externally applied $\vec{B}$ (perpendicular to plane of figure) fields. The bottom horizontal line is the position of the silicon plane. This figure is scaled to the actual size of the HPD: there is 1cm between the photocathode and the silicon plane, and each pixel is 2mm wide. At 10G, the e^- hits the pixel directly below it. At 100G, it has moved to the next pixel, and so on. This is in rough agreement with the data presented in section 4.3.

5.3 Experimental Setup

The same setup as described in chapter 3 was used to test the response of the HPD to an external magnetic field, perpendicular to the HPD's internal electric field. A large permanent U - shaped magnet (see figure 5-2) was placed over the HPD, so that the field was oriented as shown in figure 5-1. In this way, there was an electric field $\vec{E} = (0, E_y, 0)$ created by the -12 kV, and a magnetic field that was approximately $\vec{B} = (0, 0, B_z)$ created by the U - magnet. The magnet was on a mount that was

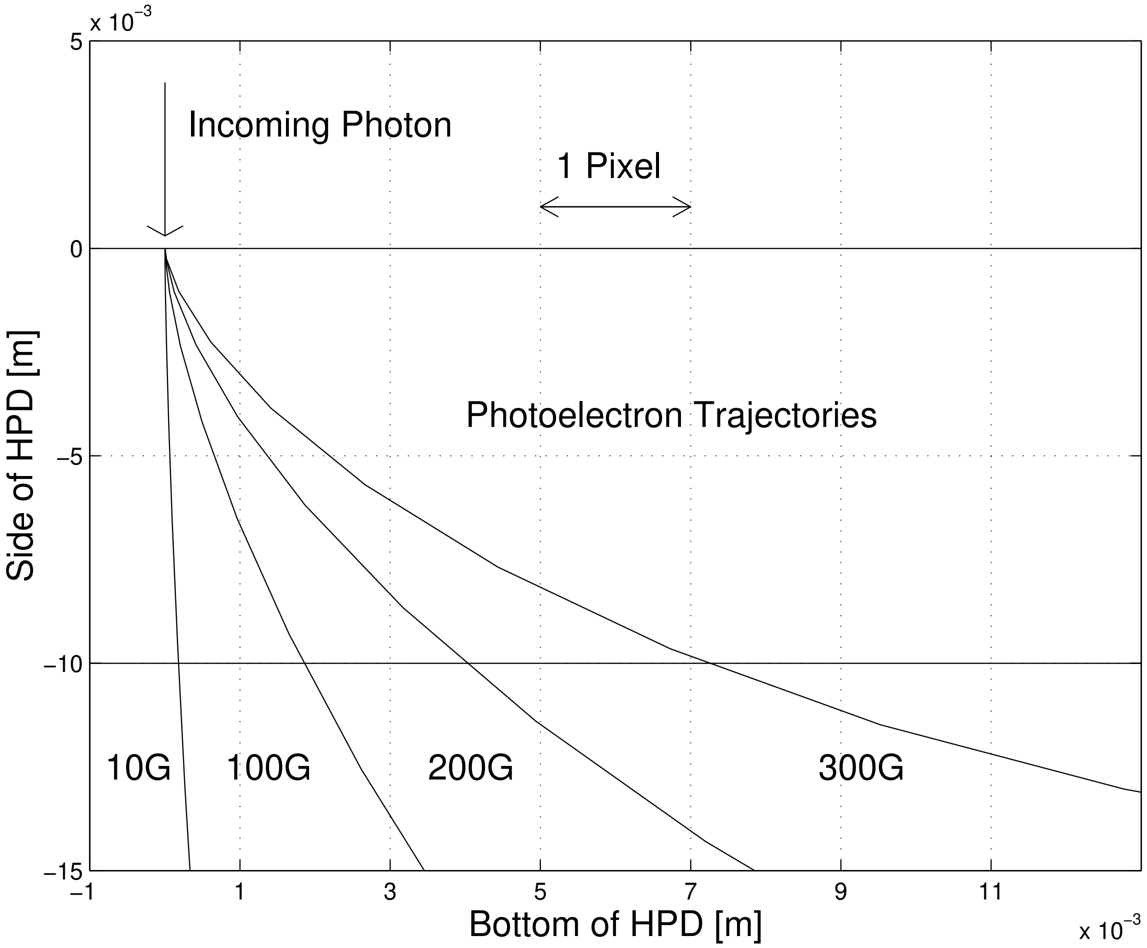

Figure 5-1: Predicted photoelectron trajectories inside HPD with $\vec{E} \perp \vec{B}$ at 12kV.

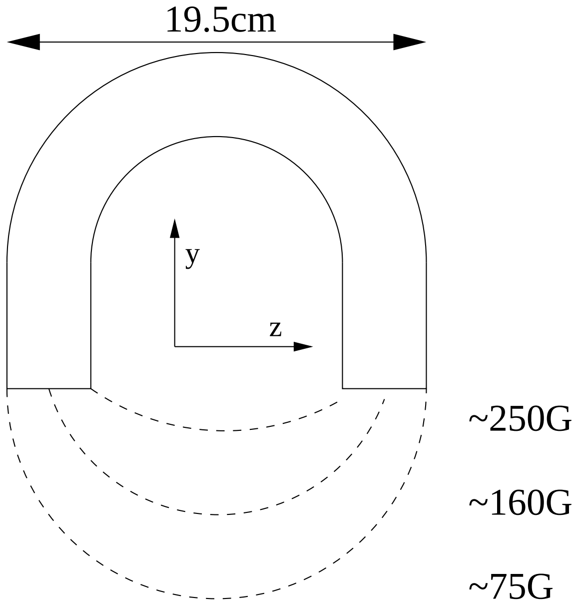

Figure 5-2: U - magnet used in magnetic field test of HPD.

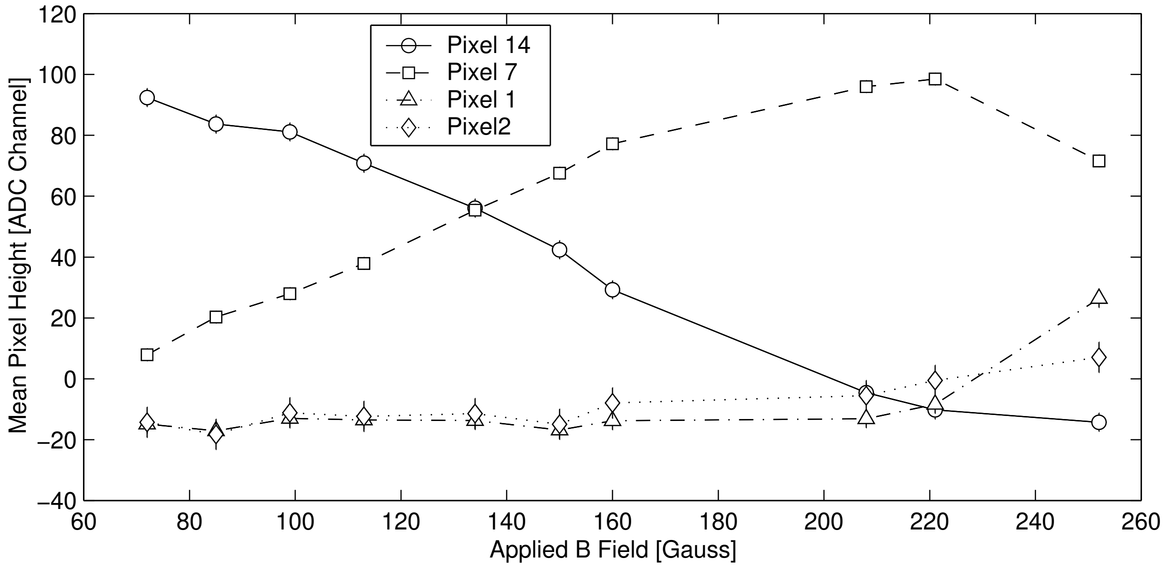

Figure 5-3: Mean ADC channel as a function of applied magnetic field.

adjustable in the $+\hat{y}$ direction. The magnet was moved up and down to get different magnetic field strengths inside the HPD. The field was measured with a radial gauss probe.

5.4 Results

The fiber optic line attached to the LED was coupled to pixel 14 (see figure 5-4 for a few of the HPD pixels), and the high voltage was set to -12kV. The applied magnetic field ranged from $\sim$ 70G to $\sim$ 250G. 1000 events (LED ON) and pedestals (LED OFF) were taken for each magnetic field. Each pixel has a different natural offset and drift, so it is necessary to take a pedestal after each measurement, and subtract it. For each field, the average ADC value of each pixel (from now on, ADC value refers to event minus pedestal) was found over 1000 events.

The average ADC value of pixels that saw photoelectrons as a function of magnetic field strength is plotted in figure 5-3. The e^-'s started out on pixel 14 ($\circ$). As the field increased, the e^-'s moved to pixel 7 (square). Then, they moved onto pixels 1 ($\triangle$) and 2 ($\diamond$). The actual position of these pixels is shown in figure 5-4. The path of the e^-'s as a function of field strength is evident from these two figures.

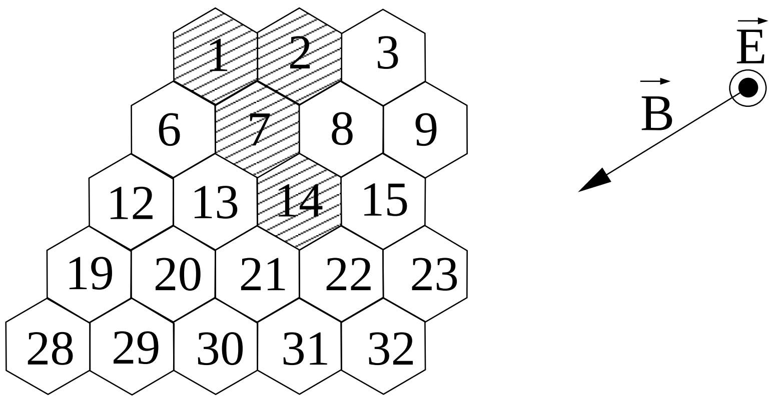

Figure 5-4: Detected path of photoelectrons over HPD pixels.

The number of e^- incident upon the entire silicon plane must be conserved as a function of $\vec{B}$, since the number of incident e^- on a pixel is proportional to the ADC value of that pixel. The mean ADC values for pixels 1, 2, 7, and 14 are summed and plotted versus $\vec{B}$ in figure 5-5. A horizontal line was fit by χ^2 minimization, giving a $\chi^2/$ d.o.f. of 5.01. The error bars were found by histogramming the 1000 events from each pixel, and then fitting this data to Gaussian distributions. The amount by which the offset parameter of the Gaussian needed to change to change the χ^2 by 1 was the error in the mean ADC value of the pixel. These translated, through averaging, to errors in the sums of pixels in figure 5-5. The best fit gave a mean ADC value of 80 channels, which amounts to 29 $\pm$ 3 photons incident upon HPD from the LED (see chapter 3, § 3.1). This is not unreasonable, since the HPD responds to individual photons.

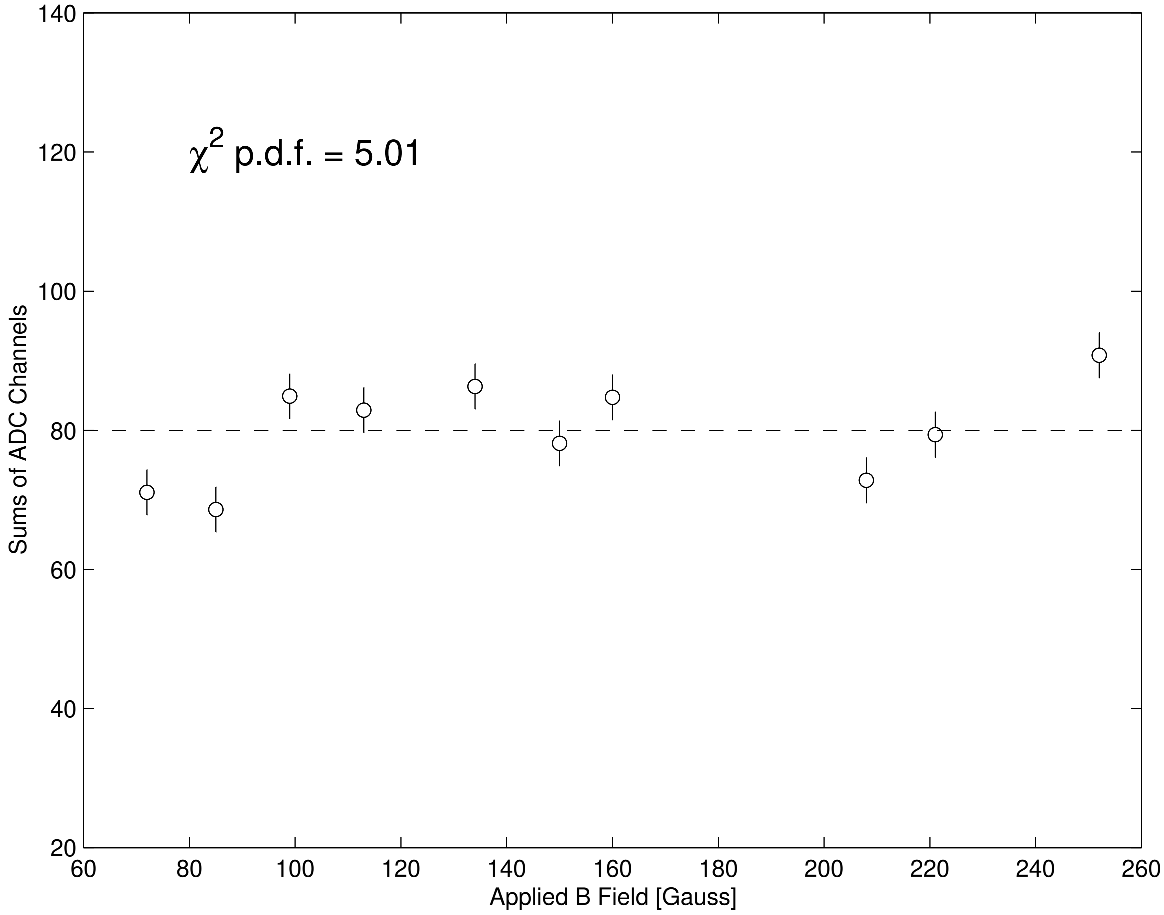

Figure 5-5: Sum of ADC counts in pixels 14, 7, 2, 1 as a function of $\vec{B}$ field.

Chapter 6

Cerenkov Imaging with the HPD

6.1 Experimental Setup

The HPD was set up in a test beam at Bates Linear Accelerator with the intention of measuring Cerenkov radiation from e^+ and e^- passing through an aerogel radiator[1].

To detect Cerenkov radiation from e^+ and e^-, the setup in figure 6-1 was constructed in the 14° area at Bates Linear Accelerator Center in Middleton, MA. γ's were produced in bremsstrahlung from a 990.9 GeV e^- beam. These photons passed through scintillator 1, bombarding a small piece of lead. This lead converted the γ's into e^+e^- pairs. These particles then triggered scintillation counter 2[2]. The particles then triggered scintillator 3 and passed through an aerogel radiator. Cerenkov radiation was produced here in a cone with central angle θ_C. The divergence of the e^+e^- pairs resulted in a negligible smearing of the Cerenkov cone.

The DAQ system was the same as described in chapter 2. A physics event trigger was two - fold coincidence between scintillators 2 and 3, where scintillator 1 was used as a veto counter. The 61 HPD pixels, whose layout is shown in figure 6-2, were read out at each physics event trigger. Immediately following a physics event, a pedestal

[1] Aerogel is a material specifically made for producing Cerenkov radiation from incident particles.

[2] Between scintillators 2 and 3, a silicon tracking system was set up in a 0.13T B field. This part of the experiment was run by another student, and was intended to test the ability of silicon detectors to track the e^+e^- pairs. Track reconstruction was underway at the time this thesis was written.

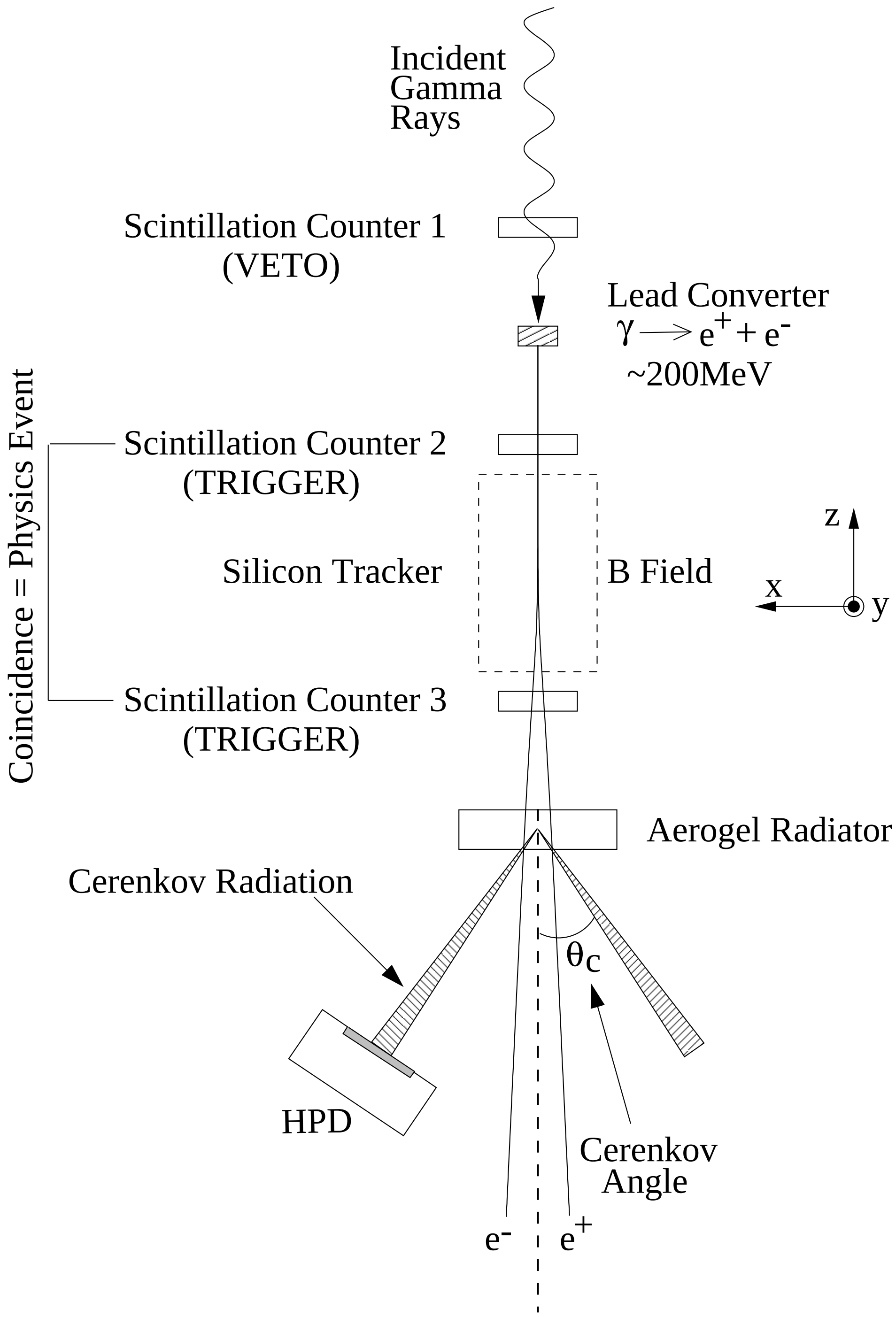

Figure 6-1: Experimental setup for Cerenkov radiation detection in Bates beam-line (not to scale).

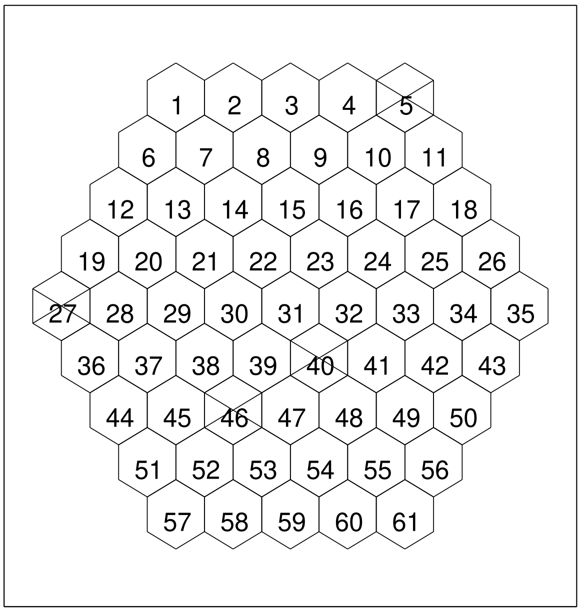

Figure 6-2: HPD Pixel Numbering (crossed out pixels were too noisy for analysis).

Run Name	Events
run025	5973
run027	9896
run028	10187
run029	1595

Table 6.1: Data runs.

event was taken to measure the noise distribution of each pixel[3]. The pixels that are crossed out in figure 6-2 were connected to noisy VA channels. Data from these pixels were not used in this analysis.

The four runs listed in table 6.1 were taken with this setup. Sample data (pixels 7, 19, 24, and 55) from run029 are shown in figure 6-3. The dotted data is pedestal data, and the solid data is physics event data. Cuts were made on these histograms, separating good events from bad events. The vertical lines are these cuts, and are explained in the next section (data left of cut is considered a Cerenkov photon hit on a pixel). Pixel 19 is typical of a pixel where incident light was indistinguishable from noise. Pixels 24 and 55 show significant light yield, and pixel 7 shows medium light

[3]Channels on the VA chip connected to the HPD have a tendency to drift.

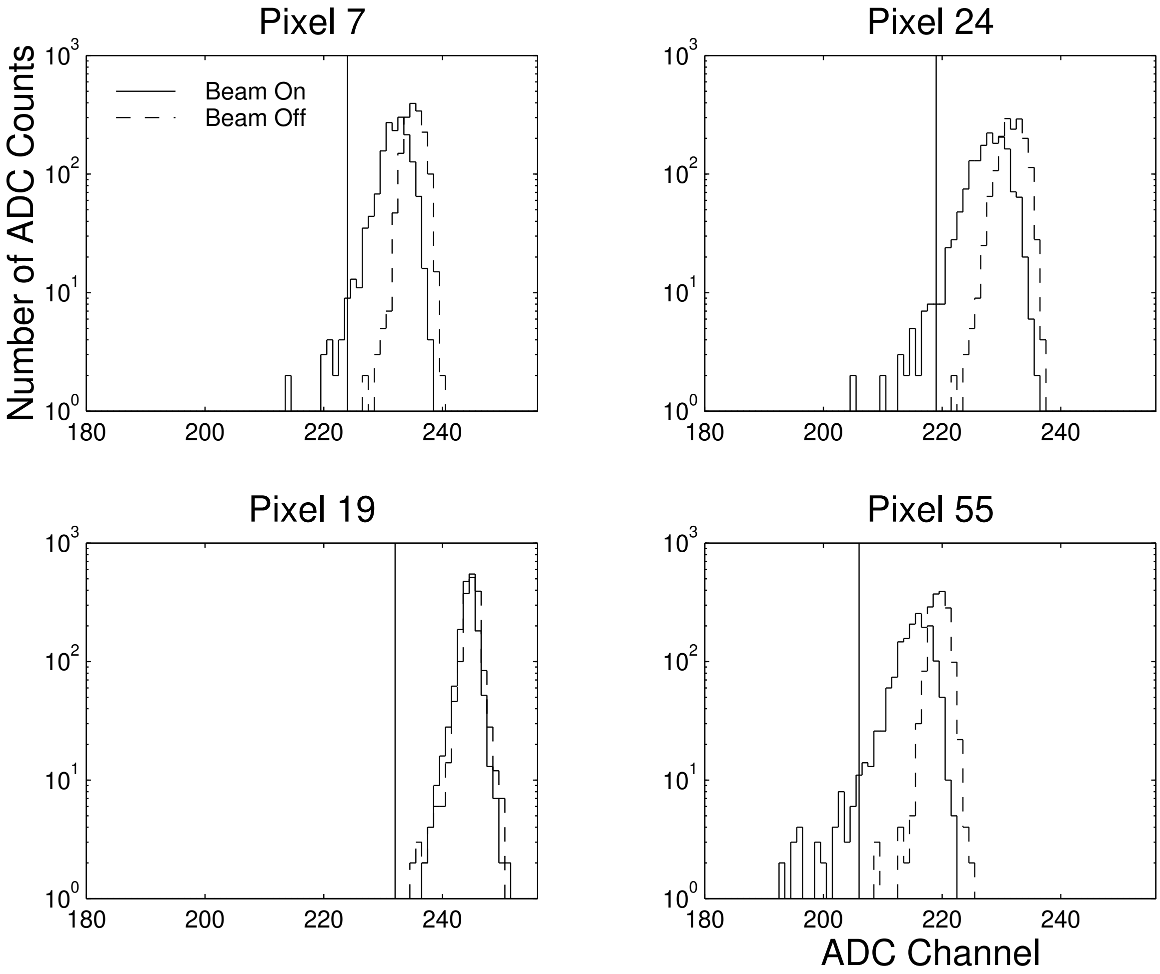

Figure 6-3: Cerenkov light data (vertical lines are data cuts).

yield. Incident light gives more counts in lower ADC bins, since the charge on the HPD was converted to a negative voltage[4] before entering the voltage ADC.

6.2 Results

6.2.1 Hit Criteria

One Cerenkov ring produces

$$N_\gamma = 500 \sin^2 \theta_C \tag{6.1}$$

[4]The repeater card has a differential output. For the calibration in chapter 3, the positive output was connected to the voltage ADC. For the Bates run, the negative output was connected. This was just chance and has no effect on the physics results.

photons [7]. Taking into account the efficiency and size of the HPD,

$$\langle N_{\gamma,HPD}\rangle = 500\sin^2\theta_C \times \frac{\epsilon l}{2\pi R} = 0.60\,\frac{\gamma}{event} \tag{6.2}$$

is the average number of expected photons incident upon the HPD per Cerenkov ring (physics event). $\epsilon = 0.20$ is the quantum efficiency of the HPD, R = 110.8mm is the average radius of a Cerenkov ring for this system, l = 18mm is the diameter of the HPD, and θ_C is the expected Cerenkov angle for the aerogel. The pixelation of the HPD compared to the size of the expected Cerenkov ring is such that on average, no curvature should be observed. Rather, strips of photons across the HPD are expected. For this reason, the diameter of the HPD is used in calculating the average number of photons incident upon the HPD, $\langle N_{\gamma,HPD}\rangle$.

Equation 6.1 was the main criteria for the cuts made on the HPD data (cuts are represented by vertical lines in figure 6-3). On pixel 7, for example, there is a clear difference between the solid and dotted histograms. The solid histogram represents the pulse height distribution of HPD pixel 7 when the Bates beam is on[5]. The dotted histogram represents the pulse height distribution when the beam is off. A cut on this data was made to distinguish Cerenkov photons from noise. The data was cut such that on average, 0.60 Cerenkov photons hit the HPD per event, as predicted by equation 6.1. For a given event, a pixel either had a hit or no hit, according to this criteria. The hit distributions of the four runs is shown in figure 6-4. The numbers in the plots are events passing cuts and total number of events.

6.2.2 Cerenkov Ring Fitting

Next, circles were fit to the data. Only events with 3 or more hits are considered good events[6]. The centers of the fit circles were constrained to be at the center of the aerogel for two reasons. First, the lack of real Cerenkov ring curvature information

[5] The beam pulsed at approximately 10 Hz. Scintillators 1, 2, and 3 told us when we had particles passing through the setup.

[6] since at least three points are needed to uniquely describe a circle.

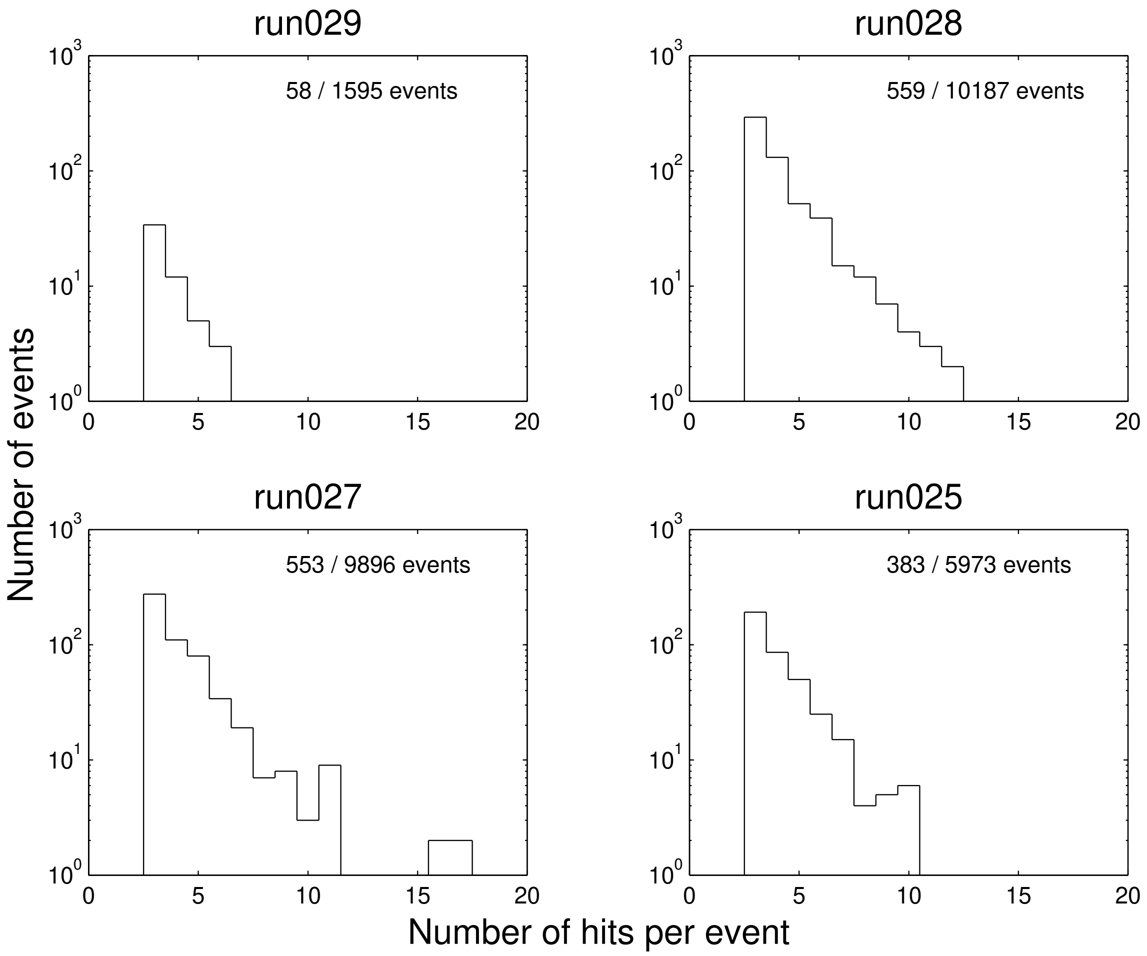

Figure 6-4: Number of hits (photons) per candidate Cerenkov ring.

expected from the HPD. Second, artificial curvature will be seen on the HPD as an artifact of the geometry of the pixels, as in figure 6-5. A straight line of photons will have some curvature on the HPD due to the discrete pixel size and placement. An event that is a candidate Cerenkov ring is shown in figure 6-5. The circle in the center is the boundary of the HPD optical window containing the photocathode. The dots are candidate Cerenkov photons. The large section of arc is the best fit circle to these points.

The distributions of fit radii are shown in figure 6-6 and listed in table 6.2. The errors on the radii listed the plots are uncertainties of the central value of the distribution (see §5.2.4 for error analysis discussion). The errors on the radii in the table include the error in the geometry of the physical setup.

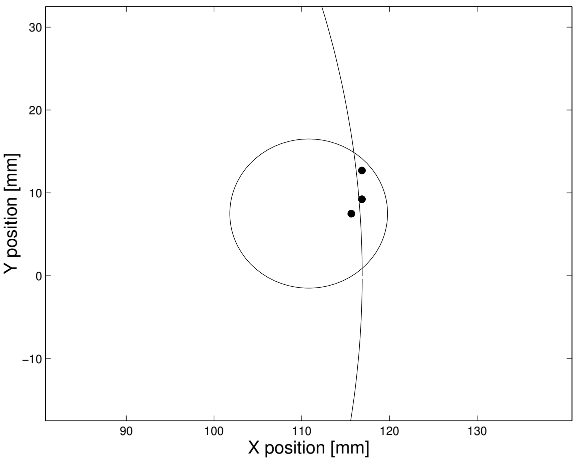

Figure 6-5: Candidate Cerenkov Ring.

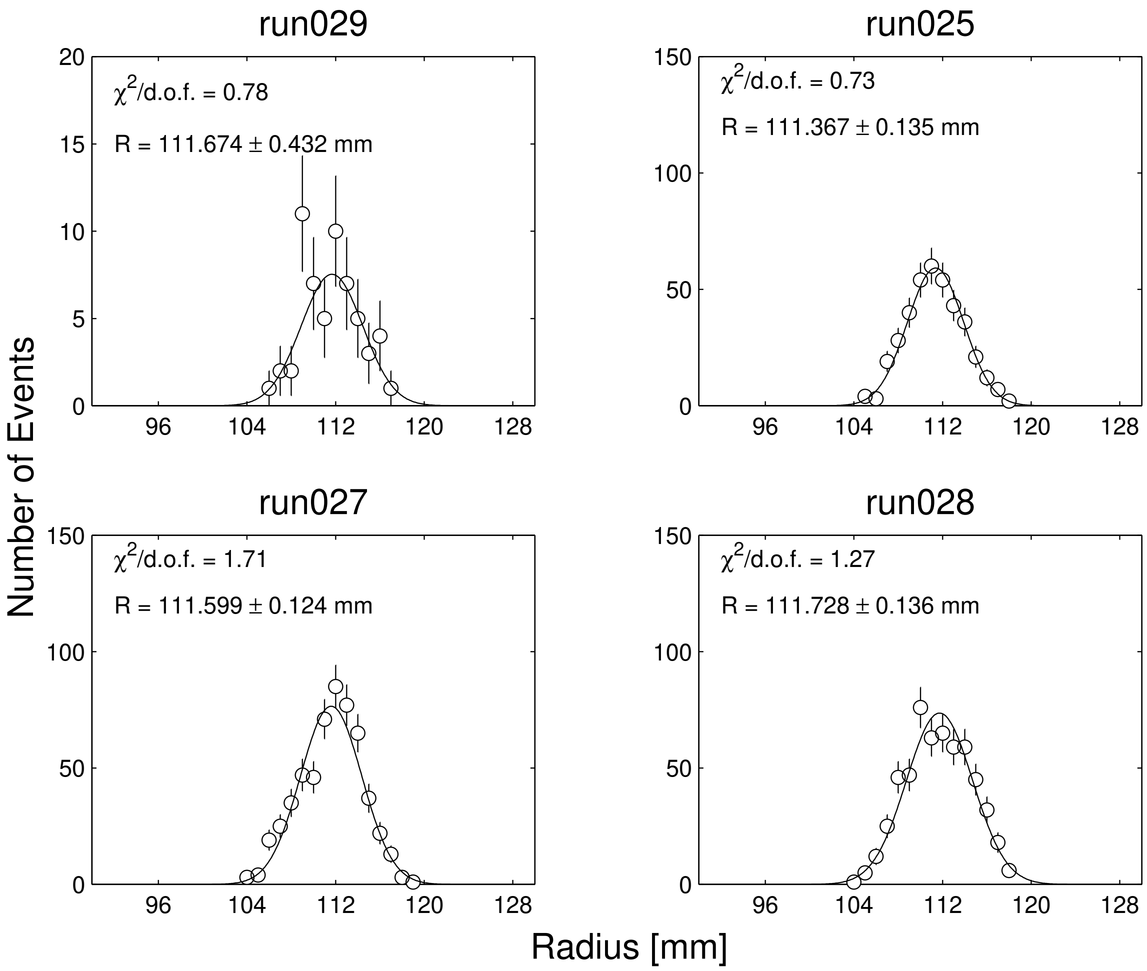

Figure 6-6: Measured distributions of Cerenkov ring radii.

Run Name	R [mm]	Δ R [mm]	Number of Events	Events after cutting
run025	111.367	1.009	5973	383
run027	111.599	1.008	9896	553
run028	111.728	1.009	10187	559
run029	111.674	1.089	1595	58

Table 6.2: Measured Cerenkov cone radius results

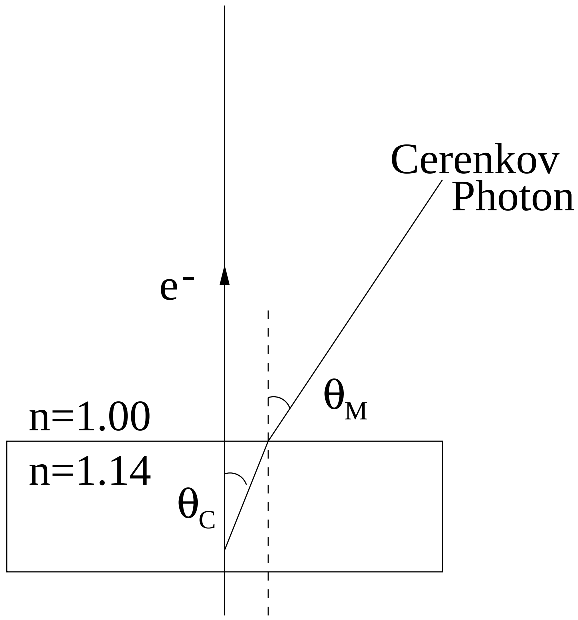

Figure 6-7: Refraction of Cerenkov photon at aerogel-air interface.

6.2.3 Extraction of θ_C and Aerogel Index of Refraction

Cerenkov photons created in the aerogel radiator will refract at the aerogel - air interface (see figure 6-7). The Cerenkov radii in figure 6-6 can be converted into a measured angle θ_M by

$$\theta_M = \tan^{-1}\left(\frac{R}{L}\right), \tag{6.3}$$

where R is the measured Cerenkov cone radius, and L is the distance from the center of the aerogel to the central plane of the HPD[7] (see figure 6-8). θ_M is the angle that

[7]The spatial accuracy of the HPD is increased with incoming light being normally incident upon the optical window, since the path of the photoelectrons inside will be affected by the angle of photon incidence. The HPD was oriented such that as Cerenkov light would be normally incident on the photocathode. During data analysis, this required a projection of each pixel's position to a plane parallel to the aerogel plane, passing through the geometrical center of the HPD optical window.

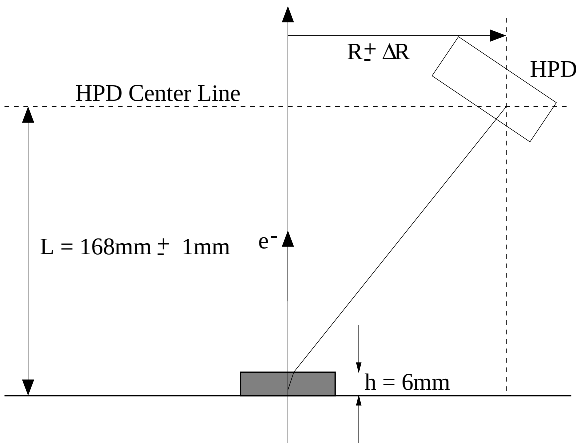

Figure 6-8: Top view of aerogel radiator (shaded) and HPD.

is actually measured by the HPD. This must be converted to the Cerenkov angle. By Snell's law, θ_M and θ_C are related by

$$n \sin \theta_C = \sin \theta_M \tag{6.4}$$

where n is the index of refraction of the aerogel. This, combined with equation 6.3, becomes

$$\theta_C = \sin^{-1}\left[\frac{1}{n}\sin\left(\tan^{-1}\left(\frac{R}{L}\right)\right)\right] \tag{6.5}$$

By the Cerenkov relation[8], a measured index of refraction is given by

$$n_{meas} = \left[\cos\left(\sin^{-1}\left[\frac{1}{n}\sin\left(\tan^{-1}\left(\frac{R}{L}\right)\right)\right]\right)\right]^{-1} \tag{6.6}$$

Since n is contained within the expression for the measured value of n, this is a consistency fit. The index of refraction for aerogel is known to be approximately 1.14. If this is the real index of refraction, then plugging this in on the right hand side of equation 6.6 and histogramming the distribution of n_{meas} obtained from the measured values of R and L should produce a distribution centered around 1.14. This would mean that the radial distributions of Cerenkov radiation are consistent with an

This is the central plane of the HPD, labelled HPD Center Line in figure 6-8.

[8]The e^- in this experiment had an energy distribution peaked at $\sim$ 200 MeV, so β is set to 1.

n = 1.14 index of refraction. These distributions are plotted in figure 6-9 and their results listed in table 6.3.

Run Name	θ_C	$\Delta\theta$	n	Δn	Number of Events
run025	29.39°	0.5°	1.147	0.005	383
run027	29.44°	0.5°	1.148	0.005	553
run028	29.46°	0.3°	1.149	0.005	559
run029	29.45°	0.5°	1.148	0.005	58

Table 6.3: Index of refraction and Cerenkov angle results using consistency fit.

6.2.4 Error Analysis

The values of θ_C and n were found by plugging in the fit values of the radii and the measured value of L into equations 6.5 and 6.6. These radii are the χ^2/ d.o.f. best fit parameters to the data. The radii distributions should be Gaussian (or Gaussian smeared by the width of the aerogel at worst) about the real Cerenkov radius. The distributions of θ_C and n from these radius distributions are not Gaussian, since there is not a linear relationship between the Cerenkov radius and these quantities. The errors on θ_C and n were propagated through equation 6.6 using the fundamental equation of error propagation

$$\sigma_n^2 = \sigma_R^2 + \sigma_L^2 \tag{6.7}$$

which becomes

$$\sigma_n = \sqrt{\left(\frac{\partial n}{\partial R}\Delta R\right)^2 + \left(\frac{\partial n}{\partial L}\Delta L\right)^2}, \tag{6.8}$$

where ΔR is found by seeing how much R has to change to achieve a $\Delta\chi^2 = 1$ for each fit, and are listed in table 6.2. ΔL = $\sqrt{10}$mm comes from geometrical considerations of the physical setup.

6.2.5 Implicit Fit of Index of Refraction

The extraction of the index of refraction in § 5.2.3 was a consistency fit. The known index was inserted as a refraction parameter in the equation for the measured index,

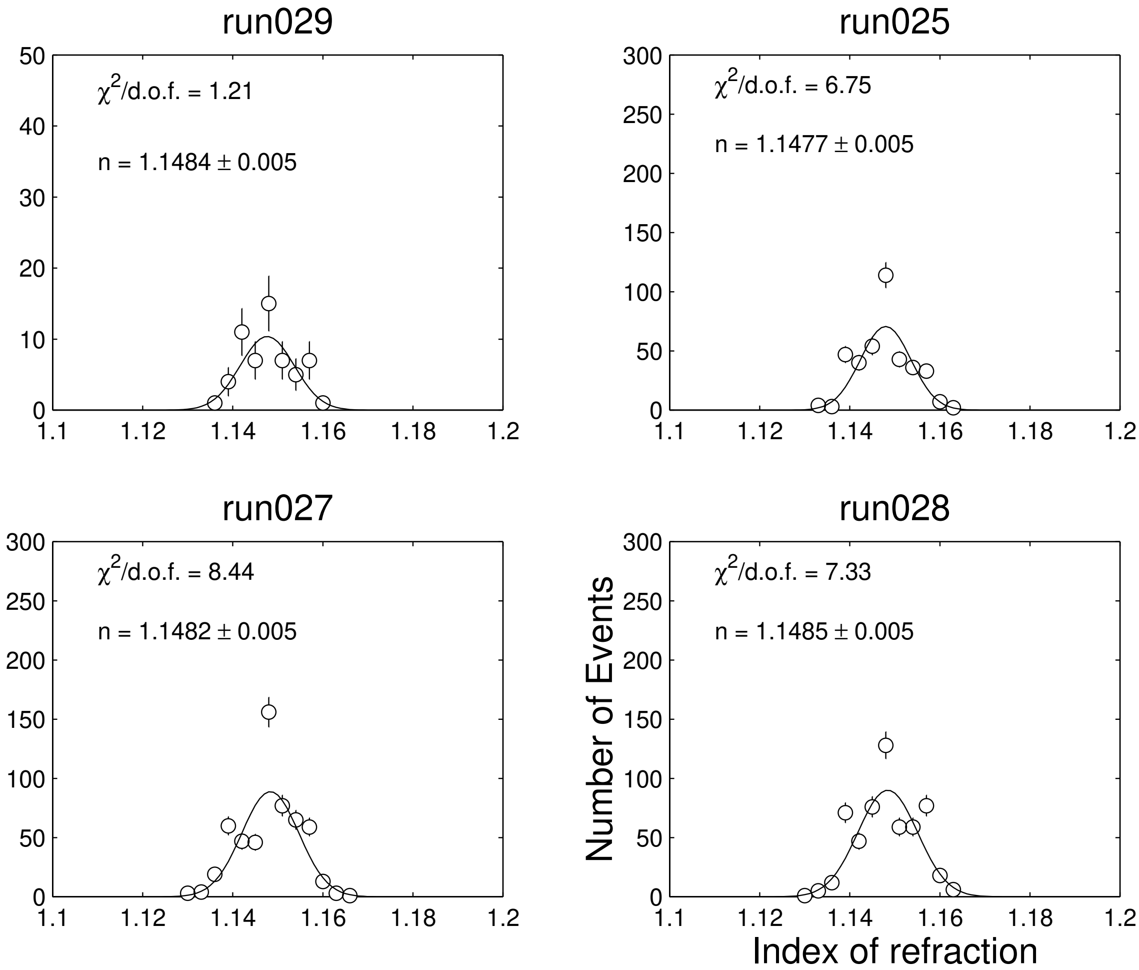

Figure 6-9: Distribution of measured indices of refraction.

and n $\pm$ Δn was extracted. It is also possible to do a simultaneous fit of the index of refraction. Equation 6.6 can be rewritten as

$$\left[\cos\left(\sin^{-1}\left[\frac{1}{n}\sin\left(\tan^{-1}\left(\frac{R}{L}\right)\right)\right]\right)\right]^{-1} - n = 0. \tag{6.9}$$

Finding the roots of this equation for the fit values of R (listed in table 6.2) and L for each set of data will give a pure measurement of the index of refraction based only on these parameters. The roots are listed in table 6.4. The errors on n were found

Run Name	n	Δn	Number of Events
run025	1.146	0.005	383
run027	1.146	0.005	553
run028	1.147	0.005	559
run029	1.147	0.005	58

Table 6.4: Index of refraction results using root finding method.

using equation 6.8.

6.3 Conclusions

A phototube study of the DEP hybrid photodiode was presented. The results of light response tests of the HPD are given in chapter 3. The HPD was exposed to various amounts of light from a green LED. From the calibration measurements presented in chapter 4, the light response of the HPD was translated to a mean photon response, as plotted in figure 4-7 in §3.2.3. The linearity of the HPD's photo response as a function of applied high voltage was also established in figure 4-5 in §3.2.2.

The ability of an HPD to function predictably in a magnetic field was shown in chapter 4. Photoelectrons inside the HPD will follow a path governed by the Lorentz force law (trajectories for various magnetic fields are shown in figure 5-1). A fiber optic line was coupled to one end of a green LED, and on the other to pixel 14 on the HPD. The voltage on the HPD was set to -12kV and a magnetic field roughly perpendicular to the internal electric field was applied. As the magnetic field was increased, the path of the photoelectrons inside the HPD curved, as shown in figures 5-3 and 5-4. The mean ADC values of the pixels in figure 5-3 are proportional to the number of photoelectrons incident upon them due to the green LED.

Lastly, the HPD was used to image Cerenkov rings produced by relativistic electrons passing through an aerogel radiator. This was done with a 990GeV electron beam at Bates Linear Accelerator Center (see figure 6-1 for the experimental setup). Four data runs were taken, producing pulse height distributions such as those shown in figure 6-3. The number of Cerenkov photons expected to be incident upon the HPD (equation 6.2) was used to cut the data into candidate events and bad events. The candidate events were hit distributions on the HPD, as in figure 6-5. These were fit to circles, producing the Cerenkov radii distributions in figure 6-6. The central value of these distributions was extracted by fitting these distributions to Gaussians. Using equation 6.6, measured indices of refraction were extracted from the radius distributions, using two separate methods (§5.2.3 and §5.2.5). The errors in the indices of refraction were obtained by propagating the error on the parameters in equation 6.6 to an error in n. The comprehensive results of this section are listed in table 6.5.

Run Name	R [mm]	ΔR [mm]	θ_C	$\Delta\theta$	n	Δn	Number of Events
run025	111.367	1.009	29.39°	0.5°	1.147	0.005	383
run027	111.599	1.008	29.44°	0.5°	1.148	0.005	553
run028	111.728	1.009	29.46°	0.3°	1.149	0.005	559
run029	111.674	1.089	29.45°	0.5°	1.148	0.005	58

Table 6.5: Comprehensive Cerenkov cone results

R is the measured Cerenkov ring radius (see figure 6-8), θ_C is the reconstructed Cerenkov cone angle, and n is the reconstructed index of refraction of the aerogel. The best fit index of refraction to these values is

$$n = 1.148 \pm 0.005 \tag{6.10}$$

The predicted indices of refraction are within the manufacturer's specifications. The HPD is able to image Cerenkov rings with millimeter and single photon accuracy.

Bibliography

[1] AMS Brochure, May 1998.

[2] Delft Electronic Products, *Multi Pixel Hybrid Photo Diodes, Technical Note.* (DEP, 1997)

[3] R. Feynman 1963, *The Feynman Lectures on Physics.* (Addison Wesley Publishing Company, 1963)

[4] P. Horowitz, W. Hill 1998, *The Art of Electronics, 2nd Ed.* (Cambridge University Press, 1998)

[5] J. D. Jackson 1999, *Classical Electrodynamics.* (John Wiley & Sons, Inc., New York, 1999)

[6] J. V. Jelley 1959, *Cerenkov Radiation and its applications.* (Pergamon Press, The Macmillan Company, New York, 1959)

[7] Ypsilantis and Seguinot, NIM A 343 (1994) 30.